HHS Public Access

Author manuscript

Cancer Res. Author manuscript; available in PMC 2018 December 01.

Published in final edited form as:

Cancer Res. 2017 December 01; 77(23): 6651–6666. doi:10.1158/0008-5472.CAN-17-0899.

EZH2 modifies sunitinib resistance in renal cell carcinoma by kinome reprogramming

Remi Adelaiye-Ogala[1,2], **Justin Budka**[3], **Nur P. Damayanti**[4], **Justine Arrington**[5], **Mary Ferris**[3], **Chuan-Chih Hsu**[5], **Sreenivasulu Chintala**[6], **Ashley Orillion**[2,7], **Kiersten Marie Miles**[8], **Li Shen**[9], **May Elbanna**[2], **Eric Ciamporcero**[10], **Sreevani Arisa**[6], **Piergiorgio Pettazzoni**[11,12], **Giulio F. Draetta**[11,12], **Mukund Seshadri**[13], **Bradley Hancock**[14], **Milan Radovich**[14], **Janaiah Kota**[15], **Michael Buck**[16], **Heike Keilhack**[17], **Brian P. McCarthy**[18], **Scott A. Persohn**[18], **Paul R. Territo**[18], **Yong Zang**[19], **Joseph Irudayaraj**[3], **W. Andy Tao**[5], **Peter Hollenhorst**[3,*], and **Roberto Pili**[1,2,6,*]

[1]Department of Cancer Pathology and Prevention, University at Buffalo, NY USA

[2]Department of Pharmacology and Toxicology, Indiana University-Indianapolis, IN USA

[3]Medical Sciences, Indiana University-Bloomington, IN USA

[4]Department of Biomedical Engineering, Purdue University, IN USA

[5]Department of Biochemistry, Purdue University, IN USA

[6]Department of Medicine, Indiana University-Indianapolis, IN USA

[7]Department of Cellular and Molecular Biology, University at Buffalo, NY USA

[8]Center for Personalized Medicine, Roswell Park Cancer Institute, NY USA

[9]Department of Medicine, Roswell Park Cancer Institute, NY USA

[10]Department of Medicine and Experimental Oncology, University of Turin, Turin IT

[11]Department of Molecular and Cellular Oncology, The University of Texas, MD Anderson Cancer Center, Houston, TX USA

[12]Department of Genomic Medicine, The University of Texas MD Anderson Cancer Center, Houston, TX

[13]Department of Pharmacology and Therapeutics, Roswell Park Cancer Institute, NY USA

[14]Department of Surgery, Indiana University-Indianapolis, IN USA

[15]Department of Medicinal and Genetics, Indiana University-Indianapolis, IN USA

[16]Center of Excellence in Bioinformatics and Life Sciences, University at Buffalo, buffalo, NY USA

[17]Epizyme Inc. Cambridge, MA, USA

[18]Department of Radiology and Imaging Sciences, Indiana University-Indianapolis, USA

[*]**Corresponding authors**: Peter Hollenhorst, PhD, Medical Sciences, Indiana University, Bloomington, IN, pchollen@indiana.edu; Roberto Pili, MD, Genitourinary Program, Indiana University-Simon Cancer Center, Indianapolis, IN, rpili@iu.edu.

Conflict of interest: Heike Keilhack is an employee at Epizyme Inc. The other authors declare no conflict of interest.

[19]Department of Biostatistics, Indiana University-Indianapolis, IN USA

Abstract

Acquired and intrinsic resistance to receptor tyrosine kinase inhibitors (RTKi) represent a major hurdle in improving the management of clear cell renal cell carcinoma (ccRCC). Recent reports suggest that drug resistance is driven by tumor adaptation via epigenetic mechanisms that activate alternative survival pathways. The histone methyl transferase EZH2 is frequently altered in many cancers including ccRCC. To evaluate its role in ccRCC resistance to RTKi, we established and characterized a spontaneously metastatic, patient-derived xenograft (PDX) model that is intrinsically resistant to the RTKI sunitinib but not to the VEGF therapeutic antibody bevacizumab. Sunitinib maintained its anti-angiogenic and anti-metastatic activity but lost its direct anti-tumor effects due to kinome reprogramming, which resulted in suppression of pro-apoptotic and cell cycle regulatory target genes. Modulating EZH2 expression or activity suppressed phosphorylation of certain RTK, restoring the anti-tumor effects of sunitnib in models of acquired or intrinsically resistant ccRCC. Overall, our results highlight EZH2 as a rational target for therapeutic intervention in sunitinib-resistant ccRCC as well as a predictive marker for RTKi response in this disease.

Keywords

renal cell carcinoma; patient-derived xenograft; sunitinib; resistance; kinome reprogramming; EZH2

INTRODUCTION

Receptor tyrosine kinase inhibitors (RTKi) such as sunitinib are presently used as standard of care in patients with recurrent metastatic renal cell carcinoma but durable responses are not common (1). (2). The clinical benefit of RTKi in RCC is thought to be mediated primarily by their anti-angiogenic effect, especially in vascular endothelial growth factor (VEGF) –driven tumors such as ccRCC. The mechanism(s) by which sunitinib harnesses angiogenesis is by targeting several receptor tyrosine kinases including VEGF receptor 2 (VEGFR2) and platelet derived growth factor receptor (PDGFR). However, recent reports from our group and others have suggested that anti-tumor effect of RTKi, such as sunitinib, may be in part independent of their anti-angiogenic effect (3–5).

Induction of multiple kinases, such as FAK, SCR, MET, FGFR2, EGFR, IGF-1R and ERBB2 has been reported to be associated with resistance to RTKi due to either transcriptional activation or post-translational upregulation (6–8). Induced kinome reprogramming can occur *via* deregulation of feedback loops and cross-talk of regulatory nodes, which in turn fosters the ability of cells to bypass the drug inhibitory effect leading to resistance (9). The kinome network can be affected by several factors including acquired mutations, stromal interactions and epigenetic modifications (10). However, there are no reports on the potential role that specific epigenetic modifications may play in reprogramming the kinome following RTKi.

Epigenetic modifications have been implicated in cancer progression and are potential drivers of drug resistance (11–16). The overexpression of EZH2 has been reported in numerous cancer types including advanced renal cell carcinoma (17–19), suggesting its role in modulating several cellular processes involved in cell survival and drug resistance (20–21). Inhibition of EZH2 has resulted in the attenuation of drug resistance in tumor and stem cells by suppressing its repressive function on target tumor suppressor genes (22). However, little is known about the epigenetic mechanisms of resistance to RTKi in RCC. We have recently reported that sunitinib resistance may be transient and be reversed by dose escalation both in selected RCC patients and tumor models, suggesting a dynamic tumor adaptation to RTKi which is likely driven by epigenetic modifications (3). The acquired resistance in the preclinical models was associated with the dynamic/reversible changes of EZH2 expression at the time of response and resistance to sunitinib. Thus, the onset of acquired resistance to sunitinib and progression may be in part due to alterations of EZH2 profiles of these tumors that provide a selective advantage to evade targeted kinase inhibition.

The approval of RTKifor advanced RCC has revolutionized the clinical treatment of this disease, though therapeutic responses are in general short lived. Understanding the mechanisms of resistance through the establishment of patient derived xenograft (PDX) models has improved our understanding of target predictions and drug response (23–28). Herein, we report the role of EZH2 in adaptive sunitinib induced kinome reprogramming in a novel, clinically relevant, metastatic PDX model of ccRCC, RP-R-02LM. Utilizing also human RCC cell line (acquired resistance) we report that sunitinib resistance is associated with increased EZH2 expression and induces global phosphorylation of kinases in both serine and tyrosine residues. Furthermore, molecular and pharmacological inhibition of EZH2 in both cells lines and PDX, respectively, attenuated the global kinase phosphorylation, increased activation of tumor suppressors and consequently re-established sensitivity to sunitinib. Taken together, these results suggest that pharmacological targeting of EZH2 is a promising strategy to overcome RTKi resistance in RCC.

Materials and Methods

Xenograft studies

Xenograft models—RP-R-01 and RP-R-02 are patient-derived xenograft (PDX) of clear cell renal cell carcinoma (ccRCC) models previously described (3,29) RP-R-02LM is a metastatic ccRCC that spontaneously metastasizes to the lungs from primary tumors implanted either subcutaneously under the skin or orthotopically in the kidney sub-capsule.

Tumor implantation—All *in vivo* experiments were approved and performed in strict accordance with the guidelines of the Institutional Animal care and use committee (IACUC) at Roswell Park Cancer Institute, Buffalo, New York and IACUC Indiana University, Indianapolis IN. Six week old homozygous ICR Severe Combined Immune-deficient (SCID) female mice were housed in a sterile, pathogen-free facility and maintained in a temperature controlled room under a 12 hour light/dark schedule with water and food ad libitum. To generate the metastatic model, RP-R-02 tumors were implanted ectopically into the prostate

of mice to select for a metastatic population. Lung metastasis developed were collected and re-implanted either subcutaneously under the skin flank or orthotopically in the kidney sub-capsule to select for pure metastatic population. For drug treatment studies, RP-R-02LM viable tumors were selected and dissected into ~1mm^2 tumor pieces and implanted either subcutaneously or orthotopically into mice. All mice were operated under sedation with oxygen, isoflurane and buprenorphine. When tumors were established and reached 50 mm^2 (subcutaneous implantation), were palpable (orthotopic implantation) or metastases were detected by imaging (micro CT), mice were randomly grouped and placed in either control group or treatment groups (n=5–20).

Drug treatment schedule—For the endpoint studies using sunitinib, bevacizumab or axitinib, mice implanted with RP-R-02LM subcutaneously (n=5–10/group) were randomly grouped into either control or treatment groups. Mice in the sunitinib treatment arm were treated with 40mg/kg 5days on 2 days off, mice in the bevacizumab treatment arm were treated with 10mg/kg two times a week and mice in the axitinib treatment arm were treated with 36mg/kg two times a week. For survival studies using sunitinib, we implanted RP-R-02LM tumor pieces (~1mm^2) into the kidney sub-capsule of 20 mice. One month after implantation, mice bearing tumors were randomly grouped into control and sunitinib treatment groups. Mice in treatment groups were treated with a dose of 40 mg/kg (sunitinib free base) (LA Laboratories, Woburn MA) 5 days on, 2 days off by oral gavage. In a second set of experiments, mice implanted with RP-R-02LM tumor pieces were grouped into control, sunitinib treated group, EPZ011989 (Epizyme Incorporation, Cambridge MA) treated group, or a combination group (n= 5/group). Mice in the sunitinib group were treated with 40 mg/kg sunitinib 5 days on/2 days off; mice in EPZ011989 treated group received 500 mg/kg EPZ011989 2x/day, 5 days on/2 days off; and the combination group received both drugs at the same dose and same treatment time.

Tumor and body weight assessment—Tumor size and body weights were assessed and recorded once a week. For tumors implanted subcutaneously, tumor size was measured once a week by caliper measurement of two diameters of the tumor (L × W = mm^2) and reported as tumor volume ((L X W^2)/2 = mm^3). Body weights were assessed using a weighing scale and recorded in grams. Endpoint tumor weights were assessed using a weigh scale and recorded in grams.

Blood and tissue collection

Tissue and blood were collected under aseptic conditions. 1 ml of blood was collected by cardiac bleeds (terminal) at the end of the experiment. Serum and plasma were separated and aliquots were stored at −80 °C for further analysis. Tumor tissues were excised, weighed and cut into sections. Sections were snap-frozen and stored in -80 °C, fixed in 10% buffered formalin, or zinc for histopathology and saved in trizol for RNA analysis.

Imaging studies

Magnetic resonance imaging (MRI)—Experimental MRI examinations were performed as previously described (30). In brief, experiments were conducted in a 4.7T/33-cm horizontal bore magnet (GE NMR Instruments, Fremont, CA) equipped with AVANCE

digital electronics (Bruker Biospec, Paravision 3.0.2; Bruker Medical Inc., Billerica, MA), a removable gradient coil insert (G060) generating a maximum field strength of 950 mT/m and a custom-designed 35-mm RF transmit receive coil. Animals were secured in a form-fitted, MR compatible sled (Dazai Research Instruments, Toronto, Canada) equipped with temperature and respiratory monitoring sensors. Animal body temperature was maintained at 37°C during imaging using an air heater system (SA Instruments Inc., Stony Brook, NY), and automatic temperature feedback was initiated through thermocouples in the sled. A phantom containing 0.15 mM gadopentetate dimeglumine (Gd-DTPA; Magnevist, Berlex Laboratories, Wayne, NJ) was used for monitoring changes in noise and system performance. Preliminary localizer images were acquired for subsequent slice prescription. Tumor volumes were calculated from multi-slice T2-weighted (T2W) spin echo images with the following parameters: Field of view (FOV) = 3.20 × 3.20 cm, matrix (MTX) = 256 × 192, slice thickness = 1 mm, NEX = 4, TR = 2500 ms, TEeff = 41.0 ms, RARE/Echoes= 8/8. Following image acquisition, raw image sets were transferred to a processing workstation and converted into Analyze™ format (AnalyzeDirect, version 7.0; Overland Park, KS). All post processing of imaging data was carried out in Analyze™ and MATLAB. A region of interest (ROI) was manually traced around the entire tumor area on each tumor slice. Tumor volume was calculated by measuring the cross sectional area on each slice and multiplying their sum by the slice thickness.

Micro Computed Tomography (CT) imaging—Respiratory gated μCT were performed at 33.63 μm on a Skyscan 1176 (Bruker, Billerica, MA) using the following scan parameters: 80 kV tube voltage; 313 mA tube current; 0.5 mm Al filter; 0.9° rotation step; no frame averaging, 4×4 binning, 32 horizontal pixel overlaps. Animals were induced and maintained with 4–5% and 1–3% isoflurane gas, balance medical oxygen, delivered at 2 mL/min, respectively. Animals were transferred to a heated carbon fiber scanning bed, landmarked, and scout scans performed to permit scan prescription of thoracic region in 2 beds. Images were reconstructed using vendor supplied filtered back-projection algorithm, using a Hamming filter (α=0.54) with a Nyquist relative cutoff frequency of 100. Post-acquisition, DICOM images were imported into Analyze™ (AnalyzeDirect, version 12.0; Overland Park, KS), registered using normalized entropy methods (31) and intensity normalized over the interval [0.0, 1.0]. Images were then segmented using constrained region growing approaches, where lung air spaces and soft tissues were defined to have values ranges of [0.0, 0.1] and [0.11, 1.0] respectively. To minimize the impact of tracheal tissue contamination on total lung volume, trachea objects were digitally removed, and object maps quantified according to the following general equation:

$$V(i) = \sum_{j=1}^{a} \sum_{k=1}^{b} \sum_{l=1}^{c} O_{Map}(i, j, k, l) * \mu(j, k, l)$$

Where V, i, j, k, l, a, b, c, O_{Map}, and μ are the volume of the *"i'th"* region, *"j'th"* object map index, *"k'th"* object map index, *"l'th"* object map index, *"a"* total number of row voxels, *"b"* total number of column voxels, *"c"* total number of slices, object map, and voxel dimension

in millimeters. Determination of lung nodules was then assessed as the reduction in lung volume for each subject with time.

In vitro assays

Cell lines—786-0 and UMRC2 cell lines from ATCC was maintained and cultured in the appropriate media supplemented with 10% FBS and 1% penicillin and streptomycin. The 786-0R (resistant cell line) was generated from the 786-0 parental line adopting a drug escalation scheme. 786-0 cells were exposed to an initial concentration of 2μM which was the concentration at which 50% of cell death was observed. When cells became resistant at 2μM, drug concentration was gradually increased by 0.5μM increments with every resistant cycle. Cells were considered resistant at ≥5μM sunitinib. UMRC2R cells were established using the same method. The period for generated resistant cells form the parental line was approximately 4 months. The IC50 at 48-hour treatment of the 786-0 and UMRC2 resistant cells was 19.9μM and 20μM, respectively. All cells are routinely tested and checked for the absence of mycoplasma. Cells were also checked to ensure that they maintained human origin by detecting the Alu sequence via PCR.

MTT and Crystal Violet Assay—786-0 and 786-0R cells were plated in six-well plated for 24 hours and treated with either DMSO (vehicle control) varying concentrations of sunitinib or a single concentration of sunitinib in combination with EPZ011989 (EZH2 inhibitor) and use MTT assay (Cayman) or crystal violet assay (Sigma) to evaluate the cells growth after 24, 48, 72 and 96 hours of treatment and absorbance read using s spectrometer (xMarks Spectrometer, Bio-Rad).

Immunohistochemistry and immunofluorescence staining

Tissue specimens were fixed for 24 hr, paraffin embedded and sectioned (4μm). Sections were de-paraffinized and rehydrated through graded alcohol washes. Antigen unmasking was achieved by boiling slides in either sodium citrate buffer (pH=6.0) or EDTA. For immunohistochemistry staining (IHC), sections were further incubated in hydrogen peroxide to reduce endogenous activity. To examine the expressions of our proteins of interest, tissue sections were blocked with 2.5% horse serum (Vector Laboratories) and incubated overnight in primary antibodies against Ki67 (1:500, Thermo Fisher), E-cadherin (1:1000, Cell Signaling), EZH2 (1:1000, Cell Signaling), H3K27me3 (1:1000, Cell Signaling) and CD31 (1:100, Dianova). Following primary incubation, tissue sections were incubated in horseradish-conjugated anti-rabbit or anti-rat antibody according to manufacturer's protocol (Vector Laboratories) followed by enzymatic development in diaminobenzidine (DAB) and counter stained in hemotoxyline. Section were dehydrated and mounted with cytoseal 60 (Thermo Scientific). For immunofluorescence staining (IF), sections were blocked with 5% BSA (Sigma), co-stained with EZH2 and either E-cadherin (1:500; Cell Signaling), pTyrosine (1:400; BioVision), pSerine (1:100), pAKT (1:400, Cell Signaling) or pFAK (1:500; Cell Signaling) and incubated overnight at 4°C. Following primary incubation, sections were incubated with either Alexa Fluor or FITC fluorochrome conjugated anti-rabbit (ThermoFisher) or anti-mouse (1:400; ThermoFisher) antibody at room temperature in a humid light-tight box. Afterwards, slides were counter stained with DABI and mounted with vectorshield mounting medium (Vector laboratories). Stained sections were analyzed

either under bright field (IHC) or under appropriate fluorescence wavelength (IF) using the EVOS FL cell imaging microscope (Life Technology) and Leica Confocal microscope (Leica). The number of positive cells was determined in a blinded fashion by analyzing four random 20x fields per tissue and quantified using Image J software.

ChIP-sequencing

ChIP was performed as previously reported (32) using 1% formaldehyde fixing and antibodies to EZH2 (5246, lot 7, Cell Signaling Technology) or H3K27me3 (9733, lot 8, Cell Signaling Technology). For sequencing, purified ChIP DNA pooled from at least three replicates was re-sheared to <150 bp in a Diagenode Bioruptor. Libraries were prepared by Truseq sample preparation (Illumina). Libraries were sequenced with a NextSeq 500 (Illumina). Sequencing reads from ChIP and input controls were aligned to the human genome (hg19) and bound regions identified using Useq (33).

RNA-sequencing

For RNA sequencing and analysis, tumor tissues and cells were collected to extract total RNA including small RNA using AllPrep DNA/RNA/miRNA universal kit (Qiagen Inc.) according to the manufacturer's protocol. RNA-seq data were de-multiplexed and aligned against the human genome (hg19) using the TopHat alignment tool. The resulting file was aligned to BAM formatted sequence alignment map utilized by the cufflinks program to estimate transcript abundance. Cufflinks generates FPKM (Fragments per Kilobase of exon per Million fragments mapped) values for every transcript allowing comparisons between samples. Differential expressed transcripts were then identified between untreated and treated samples with Cuffdiff. Gene Set Enrichment Analysis using Hallmark and Oncogenic Signatures was performed with a pre-ranked gene list from the RNA-sequencing differential analysis. The genes were ranked based on the square root of the sum of squares for the log2 (fold-change) and the magnitude of the difference between the fold changes under the two analyzed conditions. A weighting factor was multiplied with the ranking score if the treatment returned the gene toward the expression under the normal condition. For microRNA sequencing analysis, Illumina sequencing reads were de-multiplexed trimmed for adaptor sequence, and aligned to the human genome with BowTie. The aligned reads were then be mapped to miRBase and annotated miRNAs tabulated. Differential expressed miRNA was determined using the DESeq R package with parametric normalization at FDR < 10%.

Quantitative RT-PCR

Quantitative RT-PCR (qRT-PCR) was performed utilizing *EZH2*, *E-cadherin*, *SETD2*, A*LDH1A*, *HIF2a*, *E2F1*, *N-Cadherin*, *ZEB*, *VASH1*, *SNAIL* and *GAPDH* human specific primers (IDT Technologies, Sequence in Supplemental Table 1). The denaturation step was carried out at 95°C for 10 seconds; the annealing step was carried out at 58°C for 30 seconds, and extension step at 72°C for 1minute using the applied Biosystems 7900HT fast real-time PCR system (Applied Biosystems).

Time Correlated Single Photon Counting (TCSPC)-Fluorescence Lifetime Imaging (FLIM) of peptide biosensor phosphorylation

For peptide synthesis the experiments were performed as previously described (34). 786-0 and 786-0R cells were plated on cover slips in twelve-well plates for 12 hours and treated with sunitinib or DMSO for 24 hours. Afterwards, wells were washed gently 3 times with PBS and incubated with the peptide bio-sensors of interest p-VEGF-R, p-AKT, p-SCR, and p-FAK. After incubation of live cells with multiplex peptide sensors, cells were imaged using Time Correlated Single Photon Counting (TCSPC)-Fluorescence Lifetime Imaging (FLIM) to detect multiple kinase phosphorylation activity. Quantitative analysis was performed using photon decay collected from TCSPC-FLIM and fitted with multi-exponential model employing Levenberg-Marquardt algorithm to construct lifetime histogram and FLIM map.

Immunoblotting

Whole cell protein extracts from tissue and cell were denatured, separated on SDS-PAGE gels and transferred to nitrocellulose membranes. After blocking in 5% enhanced blocking agent (GE) in Tris-buffered saline–Tween, membranes were probed overnight at 4°C with the following primary antibodies: EZH2 (1:1000 dilution; cell signaling, CA USA), E-cadherin and B-Actin (1:1000, Santa Cruz). After incubation with the appropriate secondary antibody, results were detected using Western Lightning Chemiluminescence Reagent Plus according to the manufacturer's instructions (ThermoFisher Scientific) and captured on film. Quantitative measurements of Western blot analysis were performed using ImageJ and Graph-Pad software (Prism 7).

Phospho RTK array

Phosphorylation levels of multiple receptor tyrosine kinases (RTKs) were examined using the Proteome Profiler Human Phospho-RTK array kit (ARY001B; R&D Systems) following manufacturer's guidelines.

Reverse phase protein array (RPPA)

Reverse Phase Protein Array (RPPA) was performed for 12 RP-R-01 PDX tumors in this order; control (n=3), sunitinib sensitive period (n=3) and sunitinib resistant period (n=3). Slides were stained using antibodies as listed (https://www.mdanderson.org/education-and-research/resources-forprofessionals/scientific-resources/core-facilities-and-services/functional-proteomics-rppa-core/index.html) and relative protein levels were determined by fitting each dilution curve with a logistic model ('Supercurve Fitting; http://bioinformatics.mdanderson.org/OOMPA), heat map and statistical analysis was generated using Partek Genomic Suit software (Partek Inc.).

Phosphoproteomic mass spectroscopy

Cells from sunitinib sensitive and resistant cell lines were lysates and proteins denatured in 0.1% RapiGest (Waters) and further reduced with 5 mM dithiothreitol for 30 min at 50°C. Afterwards, denatured proteins were alkylated in 15 mM iodoacetamide for 1 h in the dark and then digested with proteomics grade trypsin at a 1:100 ratio overnight at 37°C. The pH

was adjusted below 3 and the sample was incubated for 45 min at 37°C. Samples were centrifuged at 16,000 × g to remove RapiGest and the supernatant was collected. Enrichment of phospho-peptide, mass spectrometric data acquisition and data analysis are previously described (35).

Clinical specimens and tissue microarray (TMA)

Tumor specimens from 101 ccRCC patients were embedded in paraffin, and established two TMA were provided by the clinical data network at Roswell Park Cancer Institute (RPCI), Buffalo New York and the Indiana University (IU) Simon Cancer Center Tissue Bank, Indianapolis, Indiana. Treatments after nephrectomy include tyrosine kinase inhibitor, VEGF blocker or mTORC inhibitors. For the overall survival, 76 metastatic (RPCI) and 25 primary (IU) tumors were analyzed. For the RTKi specific survival, 14 metastatic (RPCI) and 19 primary (IU) tumors from patients who received either sunitinib or pazopanib were analyzed. Slides stained for EZH2 (1:500; Cell Signaling) were analyzed by two pathologists and generated H-scores were used to define EZH2 status.

Statistical analysis

Data analyses are expressed as the mean ± standard error of mean (SEM). Statistical significance where appropriate was evaluated using a two-tailed student *t* test when comparing two groups or by one-way analysis of variance (ANOVA) using the student-Newman Keuls post-test for multiple comparison. A pValue < 0.05 was considered significant; *p <0.05, **p < 0.01, ***p <0.001, ns= not significant. Statistical analyses were done by GraphPad software.

RESULTS

Establishment and characterization of a novel metastatic ccRCC PDX model

To establish a metastatic ccRCC PDX model, we ectopically implanted tumor pieces from the PDX model RP-R-02 (3,34) into the anterior prostate of ICR SCID mice based on our prior experience with prostate cancer PDX that metastasize to the lungs at high frequency following intra-prostatic implantation (data not shown). All mice implanted with the tumors developed lung metastases four months post tumor implantation. Thus, we passaged the tumors from the lungs into a new set of mice. The newly established metastatic PDX model was named RP-R02LM. Surprisingly, RP-R02LM formed spontaneous lung metastases (Figs. 1A, B and Supplemental Fig. 1A) irrespective of the site of tumor implantation (subcutaneous or renal capsule). RP-R02LM tumors at the primary site, as well as the metastatic site, maintained the clear cell phenotype after several passages with a high incidence (>95%) of spontaneous lung metastases at every passage (Fig. 1C, D). In addition, PCR confirmed the presence of human Alu sequence, indicating that the tumors were human even though they are passaged in mice (Fig. 1E). The growth rate of RP-R-02LM was faster ($100mm^2$ at day 31) than the parental RP-R-02 ($100mm^2$ at day 49) (Supplemental Fig. 1B). Non-invasive MRI showed that metastatic burden was independent of primary tumor volume in mice bearing orthotopic RP-R-02LM (Supplemental Fig. 1C), suggesting that tumor shedding may occur early. In this model we observed a significant increase in *EZH2, SETD2, ALDH1A1, E2F-1* and *Snail1* expression. Evidence of epithelial-to-mesenchymal

transition (EMT) was also observed with increase in *N-cadherin, ZEB1* and *HIF2a* levels and decrease in *VASH1* and *E-cadherin* expression in RP-R-02LM compared to RP-R-02 (Fig. 1F). Immunofluorescence co-staining analysis of E-cadherin-EZH2 indicated a decrease in E-cadherin and an increase in EZH2 in the metastatic model RP-R-02LM, compared to the parental line RP-R-02 (Fig. 1G, Supplemental Fig. 1D).

RTKI induced resistance is associated with loss of anti-tumor effect but persistent anti-angiogenic and anti-metastatic activity

We have previously reported that acquired resistance to sunitinib can be transient and reversible both in preclinical and clinical studies of ccRCC (3). Thus, we wanted to assess the anti-tumor effect of sunitinib in our metastatic model. To our surprise, RP-R-02LM grown subcutaneously was intrinsically resistant to sunitinib (Fig. 2A) in contrast with the significant efficacy of sunitinib in the RP-R-02 parental model (3). However, when we investigated the effect of sunitinib on overall survival, mice treated with sunitinib had a survival benefit compared to control mice (Fig. 2B). Macroscopic and microscopic evaluations both indicated that mice following sunitinib treatment had a significant reduction of lung metastatic burden compared to the control group (Supplemental Fig. 2A). Interestingly, a close examination of the tumor vasculature showed a significant decrease in blood vessel density following sunitinib treatment (Supplemental Fig. 2B), although the percentage of proliferating cells did not change compared to the control. Similar results were observed in mice treated with axitinib, another RTKi approved for RCC patients (Fig. 2C, Supplemental Fig. 3A–C). We further investigated whether the resistance was specific to RTKi only or also to a VEGF blocker such as bevacizumab. We first confirmed that bevacizumab has an anti-tumor effect in a non-metastatic PDX model, RP-R-01 (Supplemental Fig. 4A–C). Then, we treated mice bearing subcutaneous RP-R-02LM tumors with sunitinib, bevacizumab or vehicle and found that bevacizumab, but not sunitinib had a significant anti-tumor effect as measured by growth inhibition (Fig. 2D, E). Both bevacizumab and sunitinib treatment groups showed decreased blood vessel density (Fig. 2F, G) but a reduction in proliferating cells occurred only in the bevacizumab treated group (Fig. 2F, H). A close observation of tumor metastases in the RP-R-02LM indicated an anti-metastatic effect in both sunitinib and bevacizumab treated groups, though the effect was greater in the sunitinib treated group despite the lack of control of the primary tumor (Fig. 2 I, J). This observation suggests that the anti-metastatic effect of sunitinib may be due to EMT inhibition as indicated by an increase in E-cadherin expression in tumor cells (Supplemental Fig. 4D).

Sunitinib induced resistance is associated with increased kinase activation and EZH2 mediated global kinome programming

To determine what regulatory proteins were altered with sunitinib resistance, we ran a reverse phase protein array (RPPA) on RP-R-01 PDX treated with sunitinib. The analysis identified dynamic changes in the phosphorylation of several kinases and anti-apoptotic associated proteins including, AKT, EGFR, FAK, CDK1, PI3K, JAK2, and mTORC as tumors progressed from a sensitive to a resistant state ($p>0.05$) (Fig. 3A and Supplemental Fig. 5A). To identify potential mechanisms of sunitinib resistance, we first compared sensitive (786-0) and resistant (786-0R) ccRCC cell lines. 786-0R cells were generated by

chronic *in vitro* exposure to increasing concentrations of sunitinib. We compared the level of phosphorylation activity of several kinases using specific peptide-based kinase biosensors in 786-0 and 786-0R cells. Fluorescence capture of specific kinases indicated a significant increase in phosphorylated Src ($p>0.001$), AKT ($p>0.001$), FAK ($p>0.001$) and a decrease in phosphorylated VEGFR in 786-0R cells, compared to the parental sensitive cell line 786-0 indicating a potential kinome reprogramming in the resistant cells (Supplemental Fig. 5B). Then, we compared the effect of sunitinib treatment on kinase activity in 786-0 and 786-0R cells. Surprisingly, sunitinib treatment had opposite effects in these cell lines causing loss of kinase activity in 786-0 cells, but inducing kinase activity such as AKT in 786-0R cells (Fig. 3B). Simultaneous detection of relative phosphorylated kinases using human phospho-RTK array indicated increase in phosphorylated kinases in resistant cells with sunitinib treatment (Supplemental Fig. 5C) indicating that sunitinib induces activation of alternative kinases.

To confirm the association of EZH2 expression with sunitinib exposure, we established a UMRC2 sunitinib resistant cell line and we subjected the resistant cells to drug washout before re-challenging them with sunitinib. Our immunofluorescence data indicates an increased in the intensity of EZH2 protein expression as the resistant cells were either acutely (after a 4 weeks wash out) or chronically exposed to sunitinib treatment (Supplemental Fig. 6). Similarly, we observed an increased global tyrosine and serine phosphorylation as well as increased phosphorylated FAK (Supplemental Fig. 6).

Phosphoproteomic mass spectrometry analysis in 786-0 sensitive and 786-0R resistant cells identified 3,041 phosphosites with 429 phosphosites enriched in the resistant cells, and 427 enriched in the sensitive cells by volcano plots (Supplemental Fig. 7A, B). Generated heatmap indicated changes in enriched phosphosites as cells moved from sunitinib sensitivity to drug resistance (Fig. 3C). Further analysis to determine motif enrichment using motif-x and pLOGO indicated the presence of more acidic motifs in the resistant cells as compared to the sensitive cells (Supplemental Fig. 7C). DAVID pathway analysis for these enriched phosphosites in the resistant cells revealed that the associated kinases were involved in downstream VEGF signaling pathways even though VEGF-R expression was decreased (Supplemental Fig. 8). We also identified other signaling pathways prominent with resistance (Supplemental Figs. 9 and 10). We have previously reported an association of EZH2 induction with sunitinib acquired resistance (3). To test whether the increased levels of EZH2 observed in sunitinib resistant ccRCC cells was responsible for the kinome reprogramming associated with resistance we generated EZH2 knock down cell lines using 786-0R cells (Supplemental Fig. 11A) and used immunofluorescence techniques to assess the kinome status. As expected, there was an increase in global phospho-serine and global phospho-tyrosine in the resistant cells as compared to the parental control (Fig. 3D, E). Sunitinib treatment decreased global phosphorylation in sensitive cells but significantly increased it in the resistant cells ($p=0.0014$). Similar effects on global serine phosphorylation were observed with other RTKI (Supplemental Fig. 11B). This opposite effect of sunitinib was consistent with our analysis of individual kinases and indicates a reprogramming induced by sunitinib that is unique to the resistant cells. Similar results were observed in our intrinsic sunitinib resistant *in vivo* model RP-R-02LM where immunofluorescence staining detecting global phosphorylated tyrosine and serine containing proteins revealed an increase which was abrogated by the EZH2 inhibitor EPZ011989 (36),

and further diminished in the combination treatment group (Fig. 3F). Taken together, these data suggest that EZH2 is responsible for the kinome reprogramming that occurs in sunitinib resistant ccRCC cells upon sunitinib treatment.

Sunitinib resistant cells depend on alternative kinases activation for growth which is attenuated by EZH2 inhibition

Given the dynamic changes in global phosphorylation and EZH2 role, we further determined whether these induced kinases activation led to cell survival. Using a 3D spheroid model we treated 786-0, 786-0R and 786-0R shEZH2 cells with sunitinib at different concentrations and measured cell death by propidium iodide (PI) uptake. In the parental 786-0 cells PI uptake increased ($p=0.0017$), indicating sunitinib-mediated cell death. In contrast, PI uptake in the 786-0R cells decreased upon sunitinib treatment consistently with sunitinib resistance, and potentially indicating an anti-apoptotic effect (Fig. 4A). Interestingly, 786-0R cells with the EZH2 knock down responded similarly to 786-0 cells, indicating a role for EZH2 in sunitinib resistance. Similar results were observed using another RTKi, axitinib in a conventional 2D assay, where decreased cell viability was observed with EZH2 inhibition in the resistant cell line (Supplemental Fig. 12). Thus, we compared the effect of sunitinib treatment on global phosphorylated tyrosine kinase activity in 786-0R and 786-0RshEZH2 cells by phosphoproteomic mass spectroscopy. Generated heat map indicated dynamic changes in phosphorylated tyrosine kinases in 786-0R and 786-0RshEZH2 in the presence or absence of sunitinib (Fig. 4B). Multiple tyrosine kinases phosphorylation at specific sites including FGFR2, EGFR, EPHA4/5/3, AXL and JAK1 were increased in sunitinib treated 786-0R cells. Interestingly, most the tyrosine enriched phospho-kinases were decreased in EZH2 knockdown cells and further significantly decreased in the presence also of sunitinib ($p>0.05$). In addition, FLIM peptide biosensor activity of p-AKT and p-VEGF-R2 and immunofluorescence intensity of p-FAK revealed again increased kinases activity with sunitinib treatment in resistant cells which was abrogated with inhibition of EZH2 (Fig. 4C). These observations were consistent with the results in our RP-R-02LM model (Supplemental Fig. 13A, B). Interestingly, we also observed a reversal of E-cadherin with treatment (Supplemental Fig. 13C). This observation suggests that resistant cells in the presence of sunitinib are dependent on alternative activated kinases for growth and evasion of cell death, and kinome reprogramming may enable tumor cells to escape the anti-tumor effect of sunitinib.

Sunitinib resistant phenotype is associated with a genomic EZH2 signature

To elucidate the molecular mechanism underlying EZH2 involvement in kinome reprogramming, we mapped EZH2 binding sites by ChIP next generation sequencing (ChIP-seq) in 786-0, 786-0R and 786-0RsEZH2 cells. First, we compared EZH2 occupancy across the genome in both parental (786-0) and sunitinib resistant (786-0R) cells. Using a p-value cutoff of <0.01, we identified 2344 regions bound by EZH2 in 786-0 cells and 3544 regions in the 786-0R. This significant difference indicates that the higher EZH2 expression in 786-0R cells resulted in increased genomic occupancy. Bound regions in both 786-0 and 786-0R lines strongly correlated with known EZH2/SUZ binding sites in other cell types from the ENCODE ChIP-seq data (Supplemental Fig. 14A), confirming the quality of these data. Interestingly our results showed little overlap between regions bound by EZH2 in the

786-0 and the 786-0R cells, indicating a redistribution of EZH2 binding upon resistance (Fig. 5A and Supplemental Fig. 14B). EZH2 ChIP-seq was repeated in 786-0R cells with EZH2 knockdown (786-0RshEZH2). This resulted in decreased occupancy of the regions bound by EZH2 in the 786-0R cells (Fig. 5A), but a slight increase at regions bound in 786-0 cells (Supplemental Fig. 14B) consistent with a reversal of the EZH2 redistribution. ChIP-seq of H3K27me3 indicated that this histone mark was present at regions bound by EZH2 and increased in 786-0R cells (Fig. 5A), consistent with the canonical role of EZH2 as an H3K27me3 writer. To test whether the change in EZH2 chromatin occupancy was associated with an altered gene expression program that promotes sunitinib resistance we compared RNA-seq of 786-0, 786-0R and 786-0RshEZH2. The 786-0R cells had 3174 genes that were up- or down-regulated 2-fold or more compared to the 786-0 cells. Strikingly, knockdown of EZH2 reversed these gene expression changes, with 87% of the up-regulated genes going back down, and 87% of the down-regulated genes going back up (Fig. 5B and Supplemental Table 2). Direct EZH2 target genes showed a similar reversal (Supplemental Fig. 14C). These findings indicate that EZH2 expression is a major regulator of the gene expression changes associated with sunitinib resistance in 786-0 cells. To test whether a similar phenomenon occurs in the PDX model, we performed RNA-seq of the parental RP-R-02 tumors, the metastatic RP-R-02LM tumors, and RP-R-02LM tumors from mice treated with the EZH2 inhibitor EPZ011989. In the PDX model the “return to normal” upon EZH2 inhibition was not as striking as it was when EZH2 was knocked down in the cell line model (Fig. 5B and Supplemental Table 2). This is consistent with the observation that there are multiple differences between the RP-R-02 and the RP-R-02LM tumors (i.e. both sunitinib resistance and metastasis), and thus the gene expression program mediated by EZH2 might be one of multiple changes. To compare the gene expression programs regulated by EZH2 in both cell line and tumor models, we examined the genes that change expression upon resistance and “return to normal” upon EZH2 knockdown or inhibition. These EZH2 regulated genes were associated with very similar functional categories in both the cell line and tumor system including KRAS signaling in the kidney and proteins of the apical surface of epithelial cells (Supplemental Fig. 14D). We then generated a list of 1847 genes that were differentially expressed in the sunitinib resistant cells and “return to normal” upon EZH2 inhibition or knockdown, in both the cell line and tumor systems (Fig. 5C and Supplemental Table 2). Pathway analysis of this combined gene list showed a strong enrichment for pathways related to cancer and signaling pathways associated with kinases we identified as modified upon sunitinib resistance (Fig. 5C and Supplemental Table 2).

To identify EZH2 target genes that might mediate kinome reprogramming, we specifically examined genes encoding kinases and phosphatases. Comparing all EZH2 binding sites near a kinase or phosphatase gene, we observed a dramatic redistribution of EZH2 in the resistant cells that is partially restored upon EZH2 knockdown (Fig. 5D and Supplemental Table 2). Examples of genes associated with increased EZH2 occupancy include the Ras-GAP *DAB2IP* and the phosphatase *PTPN3* (Fig. 5E). Both *DAB2IP* and *PTPN3* decrease in expression in resistant cells, but increase upon EZH2 knockdown (Fig. 5E). Both *DAB2IP* and *PTPN3* are tumor suppressors that inhibit oncogenic signaling pathways such as RAS/MAPK and PI3K/AKT (37–40). In contrast, the *PTK2* gene, which encodes the oncogenic kinase FAK, has decreased EZH2 binding in resistant cells that increases again upon EZH2

depletion (Fig. 5E). Consistently, *PTK2* expression increases in resistant cells and decreases upon EZH2 depletion (Fig. 5E). Together, these data suggest that gene expression programs associated with kinome reprogramming and EMT in both the sunitinib resistant cell line and metastatic PDX model are caused by redistribution of EZH2 across the genome and can be reversed by its inhibition.

Combination of an EZH2 inhibitor and sunitinib induces regression of established lung metastases

To assess the efficacy of a combination treatment of EZH2 inhibition and sunitinib in both primary tumor growth and metastases *in vivo*, we treated mice bearing RP-R-02LM tumors prior to tumor dissemination to the metastatic site with an EZH2 inhibitor, EPZ011989, alone and in combination with sunitinib (Fig. 6A, B). EZH2 inhibition resulted in a modest inhibition of tumor growth. Again, we did not observe a significant inhibitory effect of sunitinib on tumor growth, although there was a decrease in tumor vasculature and metastases. The greatest reduction in primary tumor burden was observed with the combination treatment. We also observed decreased metastases in the combination, although the inhibition was not greater than with single agent sunitinib (Fig. 6B, C). Then, we further investigated the effect of this combination strategy in mice with established metastases. Using micro CT imaging, we observed that single agent sunitinib did not have a significant effect on established lung metastases. Treatment with EPZ011989 resulted in smaller lung nodules. However, we observed a significant regression of the metastatic burden the mice treated with the drug combination (Fig. 6D, E). Taken together, our data provide evidence that EZH2 plays a significant role in resistance to RTKi such as sunitinib, and inhibition of its activity re-establishes drug sensitivity.

EZH2 expression correlates with metastatic disease and decreased sunitinib response in ccRCC patients

To assess whether EZH2 expression is associated with intrinsic sunitinib resistance in ccRCC patients, we utilized a TMA made with 101 samples of primary tumors from nephrectomy specimens. We performed IHC staining on the tissues to detect EZH2 and first grouped the samples into EZH2 high (H score >median) and EZH2 low (H score < median) (Fig. 7A). Kaplan-Meier survival curves generated indicated a longer overall survival (OS) in patients with low EZH2 expression (median OS 60 months) compared to patients with high EZH2 expression (median OS 19 months) ($p = 0.05$) (Fig. 7B). In a subset of 33 patients treated with RTKi we found that low EZH2 expression was associated with increased overall survival (median OS 122 months *vs* 23 months; $p=0.005$) (Fig. 7C). In addition, when we stratified into low, intermediate and high, we again observed poor survival benefit for patients with high EZH2 expression (Supplemental Fig. 15A–B).

DISCUSSION

Our findings suggest that EZH2 expression is associated with sunitinib intrinsic/acquired resistance in ccRCC *via* an adaptive kinome reprograming, and modulates the direct anti-tumor effect of RTKi. EZH2 inhibition was associated with decreased global protein phosphorylation and specific kinase activation, and restoration of sunitinib direct anti-tumor

effect both *in vitro* and *in vivo*. These findings provide a rationale for the clinical testing of combination strategies with EZH2 and RTKi in ccRCC.

E-cadherin plays a critical role in cell-cell adhesion in epithelial tissues, some of which includes cell transformation, tumor development and progression. The loss of function of E-cadherin is generally associated with increased expression of *N-Cadherin*, *ZEB* and *SNAIL*. *ZEB* and *SNAIL* mediate EMT allowing cells to detach from tumor and migrate to secondary site (41). Our qRT-PCR data revealed an increase in *N-cadherin*, *ZEB* and *SNAIL* in the metastatic model. A significant increase in HIF2α was observed in the RP-R-02LM. Increase in HIF2α has been reported to correlate with gene signatures of EMT in lung cancer models (42). We also observed an increase in expression of metastasis associated genes *ALDH1A*, *E2F-1*, *SETD2* and *EZH2* (42–45). To our knowledge, RP-R02LM is the first ccRCC PDX model with high incidence of spontaneous lung metastases to be reported in the literature, and therefore represents a valuable tool to study the molecular mechanisms involved in disease progression and for drug development.

The human kinome contains proteins kinases that comprise 1.7% of the human genome (46). Protein phosphorylation modulates enzyme localization and activity involved in several processes including cell cycle, angiogenesis, proliferation and differentiation (47). Among the protein kinases, tyrosine kinases, specifically RTKs such as VEGFR, HER/EGFR, PDGFR and FGFR have been associated with cancer progression. Several mechanisms have been proposed for the acquired/intrinsic resistance to anti-VEGF agents in ccRCC, including alternative pathway activation (i.e. c-MET and AXL) (7) and EMT (48). Targeting specific kinases and signaling networks critical for tumor growth may evoke adaptive kinome response that may bypass the primary drug target and activate or up-regulate alternative kinase signaling networks. Our reverse phase protein microarray data highlighted several proteins with increased expression in PDX tumors at the time of resistance to sunitinib. Interestingly, the majority of these kinases and receptor kinases analyzed were increased, although, as expected, the expression of sunitinib-targeted kinases, such as VEGF-R2 TK, was decreased. Other pro-survival proteins or downstream signaling proteins were expressed with resistance. Following the results from our RPPA on the activation of alternative kinases and RTKs, we performed phosphoproteomic analysis of phosphosites by MS, and assessed the phosphorylating activity of selected kinases in sensitive and resistant cell lines by fluorescence life imaging (FILM). This analysis confirmed the increased expression levels of alternative kinases as a result of sunitinib-induced resistance. The data from FILM of kinase peptide bio-sensors, which measures the phosphorylating activity of kinases, suggest that alternative kinases such as AKT, FAK, and Src had an increased phosphorylating activity in the resistant cell line. After a complete sunitinib washout phase in the resistant cells followed by re-exposure to sunitinib, we observed an increase in p-AKT in the re-exposed sunitinib treated cells compared to the control, confirming an activation of an alternative kinase with resistance to sunitinib. In addition, from all 3,041 phosphosites identified by phosphoproteomic mass spectroscopy, 429 phosphosites were enriched in the resistant cells and 427 were enriched in the sensitive cells. While the differences between sensitive and resistant cells were not significant, further motif analysis indicated an increase in the presence of acidic motifs in the resistant cells. Acidic motifs have been identified as potential downstream substrates of receptor tyrosine kinase signaling pathways (49). Thus,

our data suggest that induced resistance to RTKi, such as sunitinib, may be associated with an adaptive kinome reprogramming where alternative kinases are activated to compensate for the inhibition of the target receptor kinases, a phenomenon that has been reported in other cancers resistant to TKi (6, 50). Taken together, the activation of kinases in resistant 786-0R cells following re-exposure to sunitinib suggests that, in the setting of acquired resistance, RTKi may indeed act as activators rather than inhibitors.

Recent reports have suggested that cells in an “epigenetic poised” state may be associated with drug resistance (51). This state has the potential to revert back to non-tolerance if the epigenetic effect is inhibited. Our models of acquired (786-0R) and intrinsic (RP-R-02LM) resistance were associated with an increased expression of EZH2 suggesting a possible epigenetic mechanism. Indeed, increased global phosphorylation at tyrosine and serine residues was associated with increased EZH2 expression in the resistant phenotype. More interestingly, sunitinib treatment further increased global phosphorylation and co-localization with EZH2 suggesting that EZH2 may be interacting post-translationally with kinases leading to the stability of their expression and activity. Recent studies have reported that inhibition of epigenetic modulators can hinder the adaptation to an induced kinase reprogramming (6, 52). We found that the higher EZH2 levels in sunitinib-resistant cells correlated with novel EZH2 chromatin occupancy and increased H3K27 tri-methylation. Furthermore, knockdown of EZH2 largely reversed gene expression changes associated with resistance. To elucidate the molecular mechanism of EZH2 involvement in kinome reprogramming, we mapped EZH2 binding sites in 786-0, 786-0R and 786-0RshEZH2 cells and specifically examined genes encoding kinases and phosphatases. Our data indicated a dramatic shift in EZH2 enriched sites as cells moved from sensitivity to resistance. In the resistant cells we saw increased EZH2 occupancy at some genes, such as *DAB2IP* and *PTPN3*. However, we observed loss at others, indicating redistribution, rather than simply more EZH2 binding. In particular, EZH2 binding decreased in resistant cells at the gene (*PTK2*) encoding Focal Adhesion Kinase (FAK). In the past several studies have reported FAK to play a crucial role in mediating tyrosine phosphorylation of proteins, in some cases function as a scaffold in various signaling events and its interaction with EZH has been shown to play a crucial role in disease progression (53). Interestingly, our RPPA data also indicated an increase in FAK expression in the resistant models. Upon knockdown of EZH2 we observed a significant decrease in FAK expression at the gene level. In addition, immunofluorescence analysis indicated a significant decrease in pFAK in both 786-0RshEZH2 and RP-R-02LM treated with EZH2 inhibitor. FAK has also been shown to interact with PI3K, activating the PI3K/AKT pathway (54). Although our ChIP data showed no enrichment for AKT, protein expression analysis indicated an increase in pAKT which was attenuated upon inhibition of EZH2i which indicates the possible role of FAK mediating PI3K/AKT signaling pathway. Interestingly, pathway analysis identified PI3K/AKT signaling pathway as one of the top altered pathways. Our data indicates that a possible mechanism by which EZH2 affects kinome reprogramming is through modulation of kinases such as FAK at the transcriptional and post translational levels. Targeting EZH2 provides the mechanism by which inhibition of EZH2 may modulate kinome reprogramming.

EZH2 has been reported to be associated with aggressive disease and poor survival in RCC patients (18) (55). Our data confirm the clinical relevance of EZH2 by showing a shorter

overall survival in ccRCC patients with high EZH2 expressing tumors. Interestingly, a subset of ccRCC patients who have received RTKi had an even greater difference in overall survival if EZH2 was over-expressed in the primary tumors as compared to patients with low levels of EZH2. Though, we recognize that these results are limited due to the small sample size and validation in a larger cohort of patients is needed. However, all together, these clinical data suggest that EZH2 not only represent a potential target for therapeutic interventions, but also a possible predictive marker to identify those patients who may not benefit from RTKi. Prospective clinical studies will be required to confirm this hypothesis.

In conclusion, our results suggest that sunitinib resistance in ccRCC may be due in part to a compromised direct anti-tumor effect which appears to be modulated by EZH2. Adaptive kinase reprogramming resulting from resistance to small molecule RTKi such as sunitinib may be associated with epigenetic modulators that up regulate alternative kinases as an escape mechanism to tumor survival. We anticipate that our findings will be of immediate clinical relevance since EZH2 inhibitors are already in advanced clinical development and may be combined with RTKi to overcome/delay drug resistance in ccRCC.

Supplementary Material

Refer to Web version on PubMed Central for supplementary material.

Acknowledgments

We want to thank Epizyme Inc. for providing the EZH2 inhibitor EPZ011929. We would like to acknowledge Brian Gillard, Dr. Swathi Ramakrishnan, and Mr. Sheng-Yu Ku for assisting with maintenance of the metastatic model. We would like to acknowledge Dr. George Sandusky, Mr. Mitchel Nettleton, Mr. Max Jacobsen and the Indiana University pathology core. We are grateful for the following shared resource facilities: Mouse Tumor Modeling Resources (MTMR) and Translational Imaging Share Resource at RPCI, NY, RPPA Core Facility MD Anderson TX, Imaging Core Facility Indiana University IN, Bindley Bioscience Imaging Facility Purdue University IN, Genomics Core Facility Indiana University Indianapolis IN, Indiana Center for Biological Microscopy, Indiana University Indianapolis IN, Next-Generation Sequencing & Expression Analysis Core University at Buffalo NY, and the clinical data network (CDN) Roswell Park Cancer Institute, Buffalo NY.

Financial support: This research was funded by Roswell Park Cancer Institute's Cancer Center Support Grant from National Cancer Institute, NIH P30CA016056 (RP) and a generous donation by Richard and Deidre Turner (RP). This investigation was conducted in-part in a facility constructed with support from Research Facilities Improvement Program Grant Number C06 RR020128-01 from the National Center for Research Resources, National Institutes of Health.

References

1. Albiges L, Choueiri T, Escudier B, Galsky M, George D, Hofmann F, et al. A systematic review of sequencing and combinations of systemic therapy in metastatic renal cancer. Eur Urol. 2015; 67:100–10. [PubMed: 24841777]
2. Porta C, Paglino C, Grunwald V. Sunitinib re-challenge in advanced renal-cell carcinoma. Br J Cancer. 2014; 111:1047–53. [PubMed: 24800947]
3. Adelaiye R, Ciamporcero E, Miles KM, Sotomayor P, Bard J, Tsompana M, et al. Sunitinib dose escalation overcomes transient resistance in clear cell renal cell carcinoma and is associated with epigenetic modifications. Mol Cancer Ther. 2015; 14:513–22. [PubMed: 25519701]
4. Ciamporcero E, Miles KM, Adelaiye R, Ramakrishnan S, Shen L, Ku S, et al. Combination strategy targeting VEGF and HGF/c-met in human renal cell carcinoma models. Mol Cancer Ther. 2015; 14:101–10. [PubMed: 25381264]

5. Gotink KJ, Broxterman HJ, Honeywell RJ, Dekker H, de Haas RR, Miles KM, et al. Acquired tumor cell resistance to sunitinib causes resistance in a HT-29 human colon cancer xenograft mouse model without affecting sunitinib biodistribution or the tumor microvasculature. Oncoscience. 2014; 1:844–53. [PubMed: 25621299]
6. Stuhlmiller TJ, Earp HS, Johnson GL. Adaptive reprogramming of the breast cancer kinome. Clin Pharmacol Ther. 2014; 95:413–5. [PubMed: 24413269]
7. Zhou L, Liu XD, Sun M, Zhang X, German P, Bai S, et al. Targeting MET and AXL overcomes resistance to sunitinib therapy in renal cell carcinoma. Oncogene. 2016; 35:2687–97. [PubMed: 26364599]
8. Wilson C, Nicholes K, Bustos D, Lin E, Song Q, Stephan JP, et al. Overcoming EMT-associated resistance to anti-cancer drugs via Src/FAK pathway inhibition. Oncotarget. 2014; 5:7328–41. [PubMed: 25193862]
9. Lee HJ, Zhuang G, Cao Y, Du P, Kim HJ, Settleman J. Drug resistance via feedback activation of Stat3 in oncogene-addicted cancer cells. Cancer Cell. 2014; 26:207–21. [PubMed: 25065853]
10. Kampen KR, ter Elst A, Mahmud H, Scherpen FJG, Diks SH, Peppelenbosch MP, et al. Insights in dynamic kinome reprogramming as a consequence of MEK inhibition in MLL-rearranged AML. Leukemia. 2014; 28:589–99. [PubMed: 24240200]
11. Chekhun VF, Lukyanova NY, Kovalchuk O, Tryndyak VP, Pogribny IP. Epigenetic profiling of multidrug-resistant human MCF-7 breast adenocarcinoma cells reveals novel hyper- and hypomethylated targets. Mol Cancer Ther. 2007; 6:1089–98. [PubMed: 17363502]
12. Flinders C, Lam L, Rubbi L, Ferrari R, Fitz-Gibbon S, Chen PY, et al. Epigenetic changes mediated by polycomb repressive complex 2 and E2a are associated with drug resistance in a mouse model of lymphoma. Genome Med. 2016; 8:54. [PubMed: 27146673]
13. Knoechel B, Roderick JE, Williamson KE, Zhu J, Lohr JG, Cotton MJ, et al. An epigenetic mechanism of resistance to targeted therapy in T cell acute lymphoblastic leukemia. Nat Genet. 2014; 46:364–70. [PubMed: 24584072]
14. Landry CD, Kandel ER, Rajasethupathy P. New mechanisms in memory storage: piRNAs and epigenetics. Trends Neurosci. 2013; 36:535–42. [PubMed: 23827695]
15. Jaenisch R, Bird A. Epigenetic regulation of gene expression: how the genome integrates intrinsic and environmental signals. Nature Genetics. 2003; 33:245–54. [PubMed: 12610534]
16. Handy DE, Castro R, Loscalzo J. Epigenetic modifications: basic mechanisms and role in cardiovascular disease. Circulation. 2011; 123:2145–56. [PubMed: 21576679]
17. Liu L, Xu Z, Zhong L, Wang H, Jiang S, Long Q, et al. Prognostic value of EZH2 expression and activity in renal cell carcinoma: a prospective study. PLoS One. 2013; 8:e81484. [PubMed: 24312307]
18. Wang Y, Chen Y, Geng H, Qi C, Liu Y, Yue D. Overexpression of YB1 and EZH2 are associated with cancer metastasis and poor prognosis in renal cell carcinomas. Tumour Biol. 2015; 36:7159–66. [PubMed: 25877750]
19. Kim KH, Roberts CW. Targeting EZH2 in cancer. Nat Med. 2016; 22:128–34. [PubMed: 26845405]
20. Lu C, Han HD, Mangala LS, Ali-Fehmi R, Newton CS, Ozbun L, et al. Regulation of tumor angiogenesis by EZH2. Cancer Cell. 2010; 18:185–97. [PubMed: 20708159]
21. Varambally S, Dhanasekaran SM, Zhou M, Barrette TR, Kumar-Sinha C, Sanda MG, et al. The polycomb group protein EZH2 is involved in progression of prostate cancer. Nature. 2002; 419:624–9. [PubMed: 12374981]
22. Bracken AP, Pasini D, Capra M, Prosperini E, Colli E, Helin K. EZH2 is downstream of the pRB-E2F pathway, essential for proliferation and amplified in cancer. Embo Journal. 2003; 22:5323–35. [PubMed: 14532106]
23. Hashimoto K, Man S, Xu P, Cruz-Munoz W, Tang T, Kumar R, et al. Potent Preclinical Impact of Metronomic Low-Dose Oral Topotecan Combined with the Antiangiogenic Drug Pazopanib for the Treatment of Ovarian Cancer. Molecular Cancer Therapeutics. 2010; 9:996–1006. [PubMed: 20371722]
24. Chen WF, Hill H, Christie A, Kim MS, Holloman E, Pavia-Jimenez A, et al. Targeting renal cell carcinoma with a HIF-2 antagonist. Nature. 2016; 539:112–+. [PubMed: 27595394]

25. Kerbel RS. A Decade of Experience in Developing Preclinical Models of Advanced- or Early-Stage Spontaneous Metastasis to Study Antiangiogenic Drugs, Metronomic Chemotherapy, and the Tumor Microenvironment. Cancer J. 2015; 21:274–83. [PubMed: 26222079]
26. Tentler JJ, Tan AC, Weekes CD, Jimeno A, Leong S, Pitts TM, et al. Patient-derived tumour xenografts as models for oncology drug development. Nat Rev Clin Oncol. 2012; 9:338–50. [PubMed: 22508028]
27. Paez-Ribes M, Man S, Xu P, Kerbel RS. Development of Patient Derived Xenograft Models of Overt Spontaneous Breast Cancer Metastasis: A Cautionary Note. Plos One. 2016; 11
28. Oh BY, Hong HK, Lee WY, Cho YB. Animal models of colorectal cancer with liver metastasis. Cancer Lett. 2016
29. Miles KM, Seshadri M, Ciamporcero E, Adelaiye R, Gillard B, Sotomayor P, et al. Dll4 blockade potentiates the anti-tumor effects of VEGF inhibition in renal cell carcinoma patient-derived xenografts. PLoS One. 2014; 9:e112371. [PubMed: 25393540]
30. Ellis L, Shah P, Hammers H, Lehet K, Sotomayor P, Azabdaftari G, et al. Vascular disruption in combination with mTOR inhibition in renal cell carcinoma. Mol Cancer Ther. 2012; 11:383–92. [PubMed: 22084164]
31. Studholme C, Hawkes DJ, Hill DL. Normalized entropy measure for multimodality image alignment. International Society for Optics and Photonics. 1998:132–43.
32. Hollenhorst PC, Ferris MW, Hull MA, Chae H, Kim S, Graves BJ. Oncogenic ETS proteins mimic activated RAS/MAPK signaling in prostate cells. Genes & development. 2011; 25:2147–57. [PubMed: 22012618]
33. Nix DA, Courdy SJ, Boucher KM. Empirical methods for controlling false positives and estimating confidence in ChIP-Seq peaks. BMC bioinformatics. 2008; 9:523. [PubMed: 19061503]
34. Damayanti NP, Parker LL, Irudayaraj JM. Fluorescence lifetime imaging of biosensor peptide phosphorylation in single live cells. Angewandte Chemie. 2013; 125:4023–6.
35. Xue L, Wang WH, Iliuk A, Hu L, Galan JA, Yu S, et al. Sensitive kinase assay linked with phosphoproteomics for identifying direct kinase substrates. Proc Natl Acad Sci U S A. 2012; 109:5615–20. [PubMed: 22451900]
36. Campbell JE, Kuntz KW, Knutson SK, Warholic NM, Keilhack H, Wigle TJ, et al. EPZ011989, A Potent, Orally-Available EZH2 Inhibitor with Robust in Vivo Activity. ACS Med Chem Lett. 2015; 6:491–5. [PubMed: 26005520]
37. Min J, Zaslavsky A, Fedele G, McLaughlin SK, Reczek EE, De Raedt T, et al. An oncogene-tumor suppressor cascade drives metastatic prostate cancer by coordinately activating Ras and nuclear factor-kappaB. Nat Med. 2010; 16:286–94. [PubMed: 20154697]
38. Min J, Liu L, Li X, Jiang J, Wang J, Zhang B, et al. Absence of DAB2IP promotes cancer stem cell like signatures and indicates poor survival outcome in colorectal cancer. Sci Rep. 2015; 5:16578. [PubMed: 26564738]
39. Bellazzo A, Di Minin G, Collavin L. Block one, unleash a hundred. Mechanisms of DAB2IP inactivation in cancer. Cell Death Differ. 2017; 24:15–25. [PubMed: 27858941]
40. Li MY, Lai PL, Chou YT, Chi AP, Mi YZ, Khoo KH, et al. Protein tyrosine phosphatase PTPN3 inhibits lung cancer cell proliferation and migration by promoting EGFR endocytic degradation. Oncogene. 2015; 34:3791–803. [PubMed: 25263444]
41. Sanchez-Tillo E, Lazaro A, Torrent R, Cuatrecasas M, Vaquero EC, Castells A, et al. ZEB1 represses E-cadherin and induces an EMT by recruiting the SWI/SNF chromatin-remodeling protein BRG1. Oncogene. 2010; 29:3490–500. [PubMed: 20418909]
42. Kim WY, Perera S, Zhou B, Carretero J, Yeh JJ, Heathcote SA, et al. HIF2alpha cooperates with RAS to promote lung tumorigenesis in mice. J Clin Invest. 2009; 119:2160–70. [PubMed: 19662677]
43. Knoll S, Furst K, Kowtharapu B, Schmitz U, Marquardt S, Wolkenhauer O, et al. E2F1 induces miR-224/452 expression to drive EMT through TXNIP downregulation. EMBO Rep. 2014; 15:1315–29. [PubMed: 25341426]
44. Wang J, Liu L, Qu Y, Xi W, Xia Y, Bai Q, et al. Prognostic value of SETD2 expression in patients with metastatic renal cell carcinoma treated with tyrosine kinase inhibitors. J Urol. 2016

45. Zingg D, Debbache J, Schaefer SM, Tuncer E, Frommel SC, Cheng P, et al. The epigenetic modifier EZH2 controls melanoma growth and metastasis through silencing of distinct tumour suppressors. Nat Commun. 2015; 6:6051. [PubMed: 25609585]

46. Fabbro D, Cowan-Jacob SW, Mobitz H, Martiny-Baron G. Targeting cancer with small-molecular-weight kinase inhibitors. Methods Mol Biol. 2012; 795:1–34. [PubMed: 21960212]

47. Bang SM. Targeting the protein kinases for anti-cancer therapy. Korean J Hematol. 2012; 47:157–8. [PubMed: 23071467]

48. Hammers HJ, Verheul HM, Salumbides B, Sharma R, Rudek M, Jaspers J, et al. Reversible epithelial to mesenchymal transition and acquired resistance to sunitinib in patients with renal cell carcinoma: evidence from a xenograft study. Molecular cancer therapeutics. 2010; 9:1525–35. [PubMed: 20501804]

49. Lemmon MA, Schlessinger J. Cell signaling by receptor tyrosine kinases. Cell. 2010; 141:1117–34. [PubMed: 20602996]

50. Kong A, Calleja V, Leboucher P, Harris A, Parker PJ, Larijani B. HER2 oncogenic function escapes EGFR tyrosine kinase inhibitors via activation of alternative HER receptors in breast cancer cells. PLoS One. 2008; 3:e2881. [PubMed: 18682844]

51. Brown R, Curry E, Magnani L, Wilhelm-Benartzi CS, Borley J. Poised epigenetic states and acquired drug resistance in cancer. Nat Rev Cancer. 2014; 14:747–53. [PubMed: 25253389]

52. Zawistowski JS, Bevill SM, Goulet DR, Stuhlmiller TJ, Beltran AS, Olivares-Quintero JF, et al. Enhancer Remodeling during Adaptive Bypass to MEK Inhibition Is Attenuated by Pharmacologic Targeting of the P-TEFb Complex. Cancer Discov. 2017; 7:302–21. [PubMed: 28108460]

53. Zhao J, Guan JL. Signal transduction by focal adhesion kinase in cancer. Cancer Metastasis Rev. 2009; 28:35–49. [PubMed: 19169797]

54. You D, Xin J, Volk A, Wei W, Schmidt R, Scurti G, et al. FAK mediates a compensatory survival signal parallel to PI3K-AKT in PTEN-null T-ALL cells. Cell Rep. 2015; 10:2055–68. [PubMed: 25801032]

55. Hirata H, Hinoda Y, Shahryari V, Deng G, Nakajima K, Tabatabai ZL, et al. Long noncoding RNA MALAT1 promotes aggressive renal cell carcinoma through Ezh2 and interacts with miR-205. Cancer research. 2015; 75:1322–31. [PubMed: 25600645]

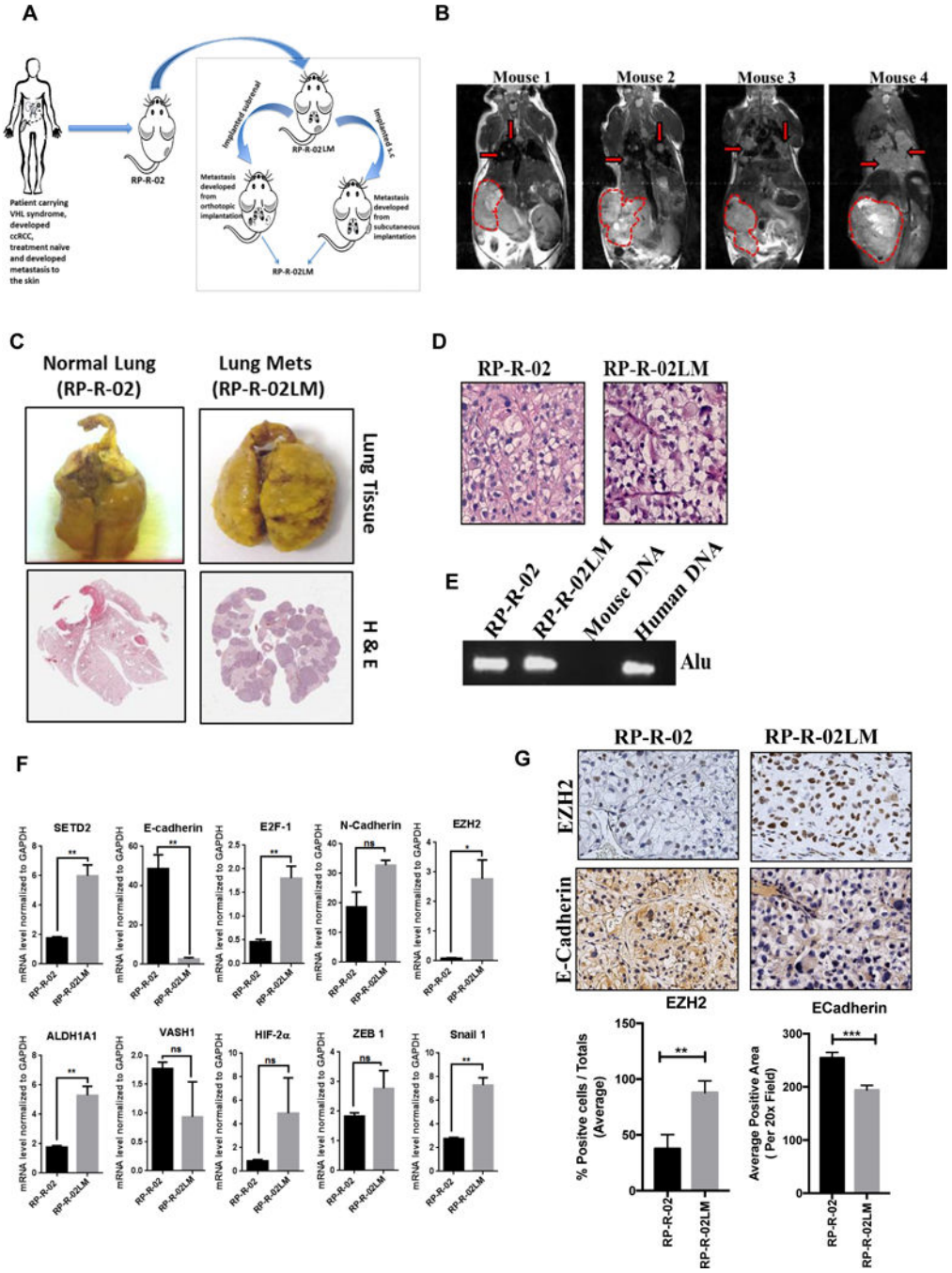

Figure 1. Characteristics of RP-R-02LM

(A) Schematic of the development of the metastatic ccRCC model, RP-R-02LM (B) Coronal T2-weighted magnetic resonance images showing primary tumor (outlined in red dotted lines) and lung metastases (red arrows) in mice with orthotopic implanted RP-R-02LM tumor. (C) Representative photographic images and H&E stained lungs of mice bearing RP-R-02LM indicate lungs metastasis compared to the parental model. (D) Representative H&E stained sections of RP-R-02 and RP-R-02LM primary PDX (subcutaneous) indicate that both models still maintain the clear cell morphology after several passages in mice (400um).

(E) PCR data indicates the presence of human Alu sequence in both the parental and the metastatic models. (F) Quantitative RT-PCR of genes associated with metastases shows an increase in *ZEB*, *HIF1α*, *N-Cadherin, STED2*, *EZH2*, *E2F1*, *Snail*, and *ALH1A1* expression, and a decrease in *E-cadherin* and *VASH1* expression in RP-R-02LM compared to RP-R-02. (*p-value = <0.01, **p-value = <0.001, ns= not significant). (F) Immunohistochemistry staining and quantification analysis of E-cadherin and EZH2 in RP-R-02 and RP-R-02LM tumors.

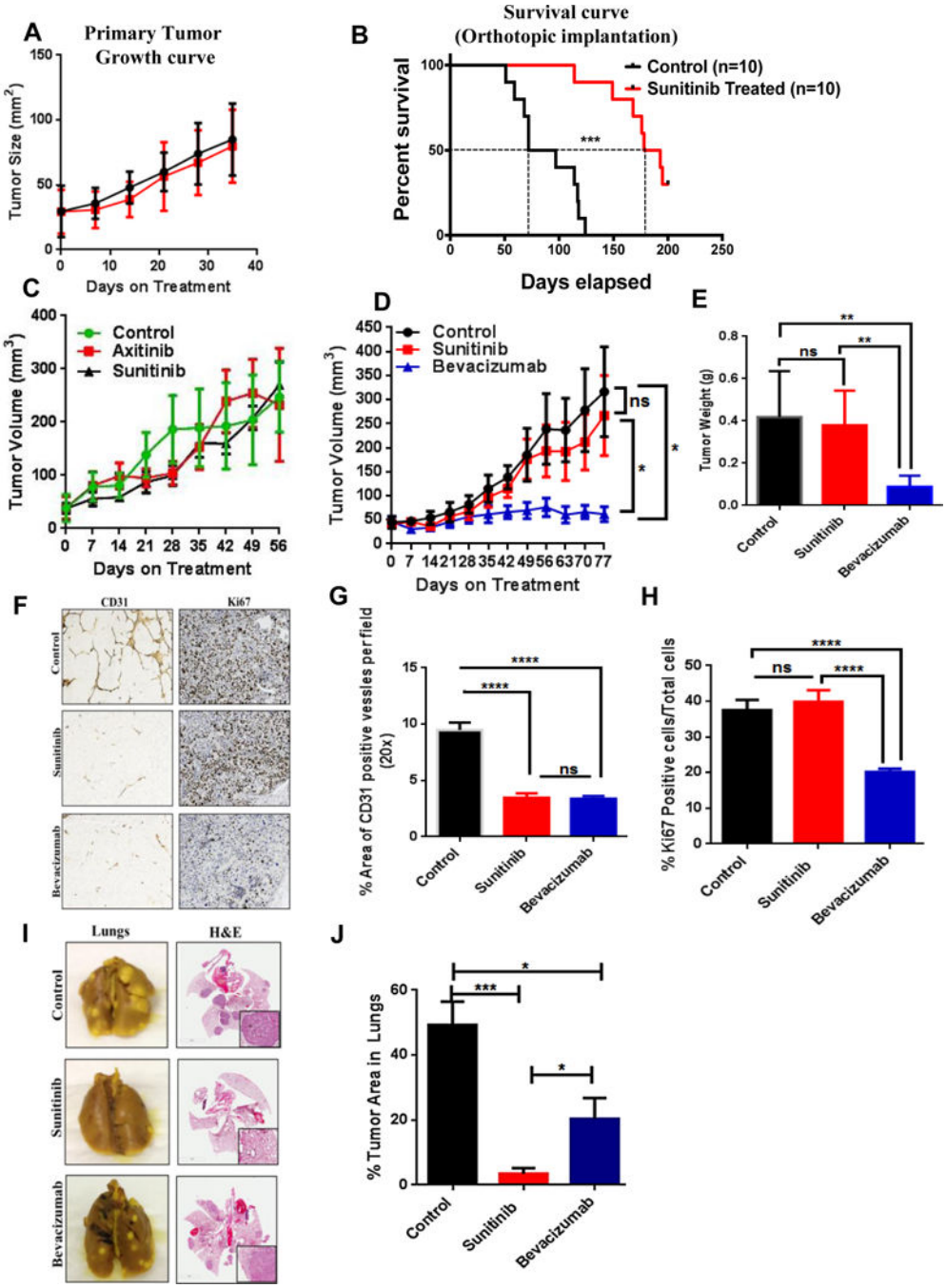

Figure 2. Sunitinib treatment fails to inhibit tumor growth in RP-R-02LM but inhibits metastases

(A) Tumor growth curves of mice treated with sunitinib had no significant difference in the growth rate compared to the control, indicating that the tumors are intrinsically resistant to sunitinib. (B) Kaplan-Meier curves showing a significant survival benefit with Sunitinib treatment compared to untreated control animals. (C) Tumor growth curve for mice untreated or treated with either sunitinib or axitinib. (D-E) Tumor growth of mice untreated or treated with either sunitinib or bevacizumab indicates a significant decrease in the bevacizumab treated group compared to sunitinib and control. (F) Immunohistochemistry

indicates decreased vessel density (CD31) with sunitinib and bevacizumab treatment but a decrease in percent of proliferating cells (Ki67) in only bevacizumab treated groups. (G,H) Graphs indicate quantitative analysis of CD31 and Ki67 in the primary tumors within each treatment group. (I) Photographic evidence of decreased metastatic burden with both sunitinib and bevacizumab treatment. (J) Graph indicates quantitative analysis of percentage of tumor burden in the lungs within each treatment group. Results are presented as mean ± SEM. *p-value = <0.05, **p-value = <0.005, ***p-value = <0.001, ns=not significant.

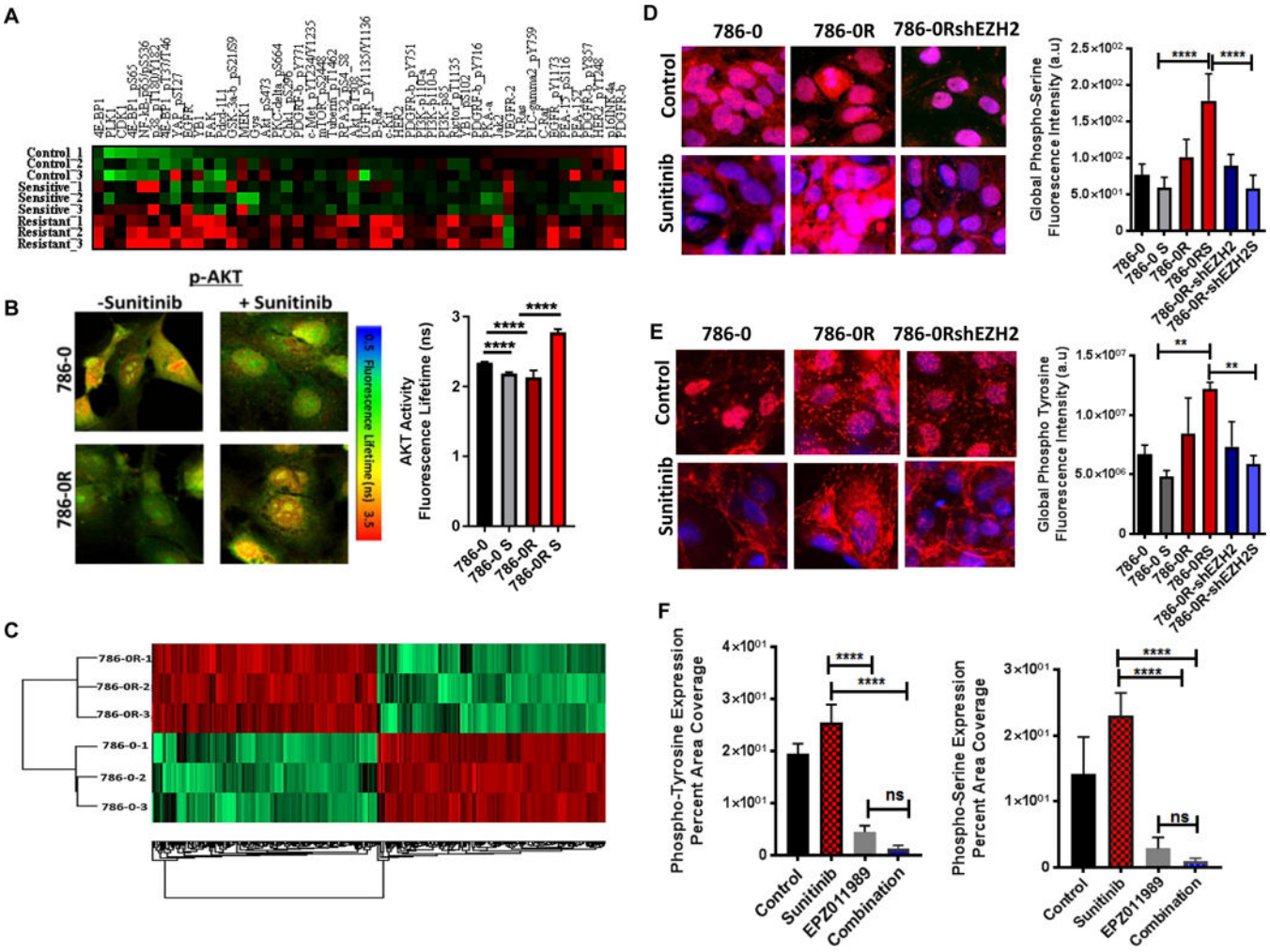

Figure 3. Sunitinib induced resistance is associated with an increase in EZH2 and alternative kinases

(A) Heatmap of selected phosphorylated kinases and proteins in RP-R-01 PDX models at the point of sensitivity and resistance to sunitinib. (B) Representative images of peptide-based kinase biosensor in sunitinib-resistant generated cells 786-0R and 786-0; Bar graphs indicating significant increase in phosphorylating activity of AKT with resistance. (C) Generated heatmap from phosphoproteomic MS analysis indicates a shift in the differential enrichment of phosphosites as cells moves from sensitivity to resistance in ccRCC cell lines. (D) Immunofluorescence staining of 786-0, 786-0R and 786-0RshEZH2 cells indicate increased global phospho-tyrosine and phospho-serine in 786-0R cells with sunitinib treatment which was attenuated with knockdown of EZH2. (E) Quantitative analysis on RP-R-02LM tumor pieces indicates a significant increase in global tyrosine and global serine phosphorylation with sunitinib treatment which is abrogated with pharmacological inhibition of EZH2 and combination with sunitinib. Results are presented as means + SEM. ****p-value = <0.0001.

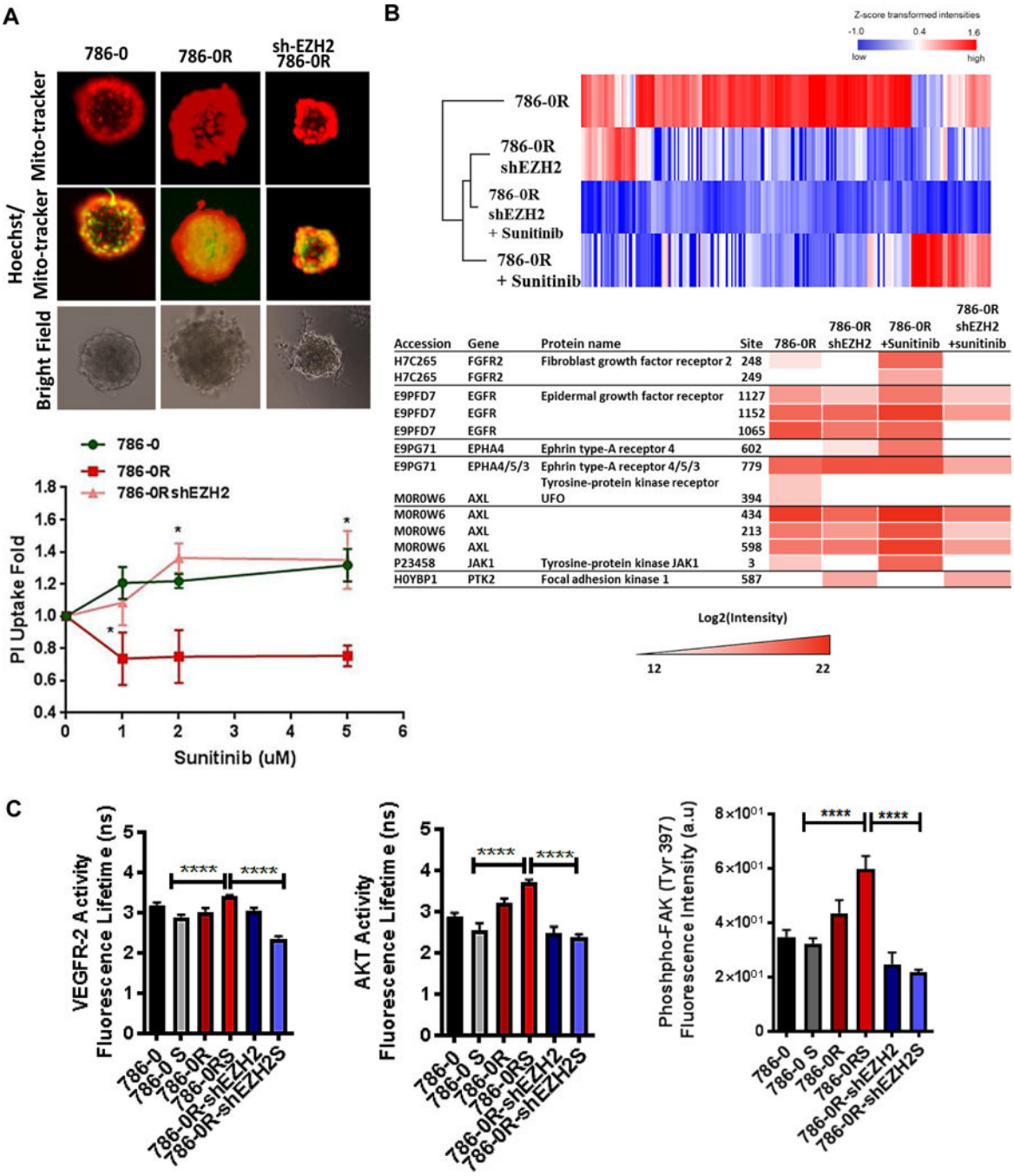

Figure 4. EZH2 inhibition diminishes induced global phosphorylation leading to sunitinib sensitivity in resistant models

(A) 3D spheroid assay indicating fold change in PI uptake in 786-0, 786-0R and 786-0RshEZH2 cells with increasing concentration of sunitinib. (B) Heatmap generated from pY enrichment analysis indicating dynamic changes in tyrosine phosphorylated kinases in 786-0R and 786-0RshEZH2 cells in the presence or absence of sunitinib. Table indicates prominent kinases that were increased with sunitinib treatment to be decreased with EZH2 inhibition. (C) Quantitative analysis of immunofluorescence intensity for p-FAK and p-AKT in 786-0, 786-0R and 786-0RshEZH2 cells revealed an increased intensity and activity with

sunitinib treatment in 786-0R cells which was significantly decreased with knockdown of EZH2. (D). Results are presented as means + SEM. ****p-value = <0.0001.

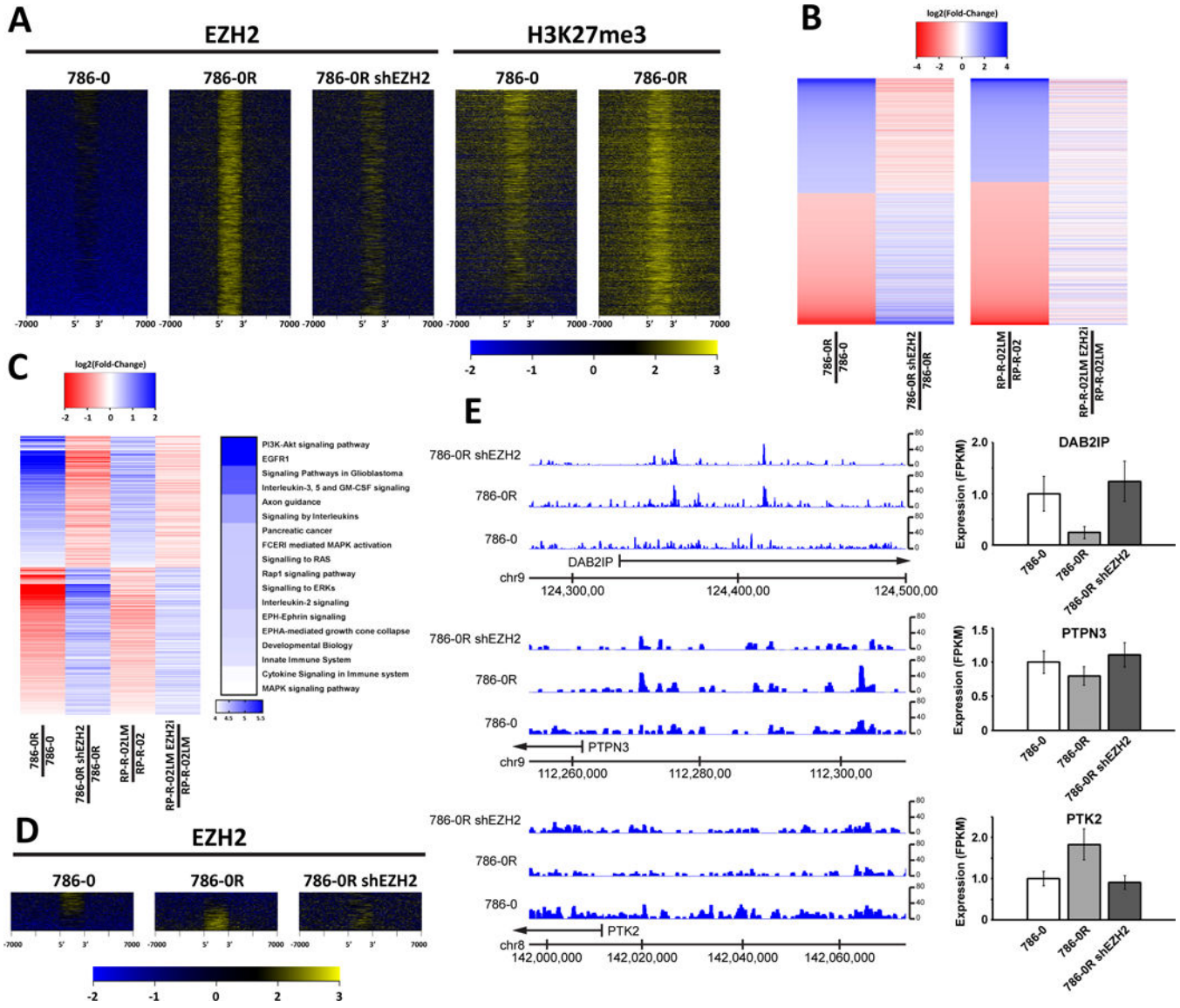

Figure 5. EZH2 expression mediates a gene expression program associated with kinome reprogramming and epithelial cell function

(A) Heatmap comparison of EZH2 or H3K27me3 ChIP-seq read counts from indicated cell lines at the 3544 regions bound by EZH2 in 786-0R cells. (B-Left) Heatmap showing all up- and down-regulated genes rank-ordered by z-score change in 786-0R cells compared to 786-0 cells and showing how expression of these genes changes upon EZH2 shRNA in 786-0R cells. (B-Right) Similarly, genes altered in RP-R-02LM tumors compared to RP-R-02 tumors are shown followed by “return to normal” upon EZH2 inhibition. (C) Heatmap displays 1847 genes that increase or decrease in expression upon resistance in both cell line and tumor system and return to normal upon EZH2 shRNA in both systems. Pathway analysis (65) of these 1847 genes indicates strong enrichment for pathways related to cancer and the kinases which were modified upon sunitinib resistance. (D) Heatmap depicts EZH2 bound sites near kinase and phosphatase encoding genes in 786-0, 786-0R and 786-0RshEZH2. (E) ChIP-seq tracks and bar charts for *DAB2IP*, *PTPN3* and *PTK2* show

gain or loss of EZH2 binding that correlates with gene expression changes measured by RNA-seq (n=2, error bars show 95% confidence interval).

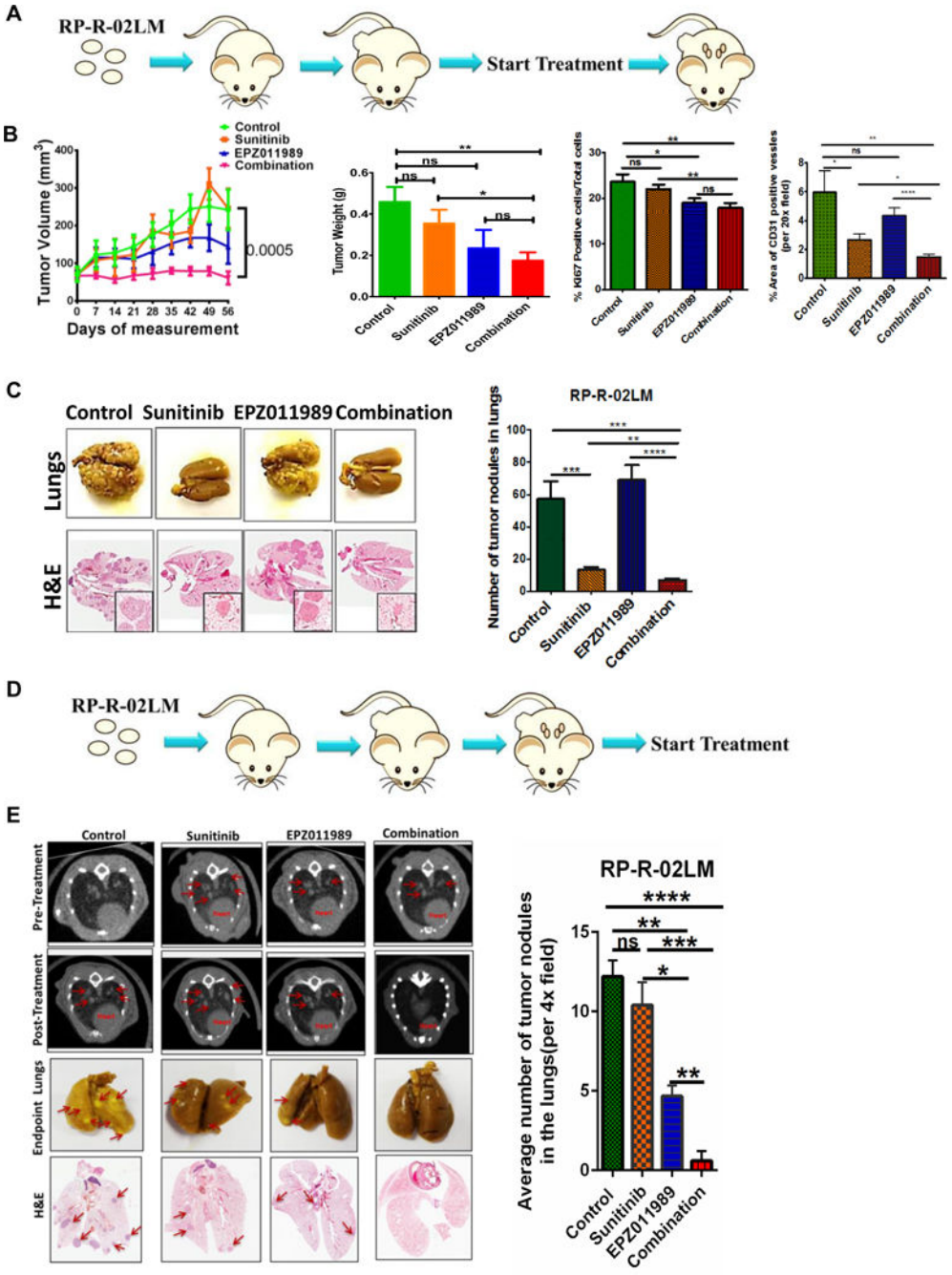

Figure 6. Combination of EZH2 inhibitor and sunitinib overcomes sunitinib resistance

(A) Schema representation of *in vivo* study and time of treatment prior to development of metastases is depicted. (B) Tumor growth curve assessed by blinded measurements using calipers, endpoint tumor weight, and decreased percentage of vessel density and proliferating cells (4 random fields/tissue 20X magnification) indicates an overall decreased in tumor burden in the combination group. (C) Representative photographic evidence and H&E images of lungs in each group indicates a significant decreased in metastatic burden in sunitinib treated group and the group treated with combination of both drugs. (D) A schema

representation of *in vivo* studies treated after development of metastases. (E-Right) Representative micro CT images (1st & 2nd panel), photographic images (3rd panel) and H&E staining (4th panel) of lungs with or without treatment indicate a significant decrease of metastases in combination treatment compared to controls and single agent. (E-left) Quantification of tumor nodules in the lungs indicates a significant decrease in the combination group. Results are presented as means ± SEM, *p-value = <0.05, **p-value = <0.005, ***p-value = <0.001 and ns=not significant.

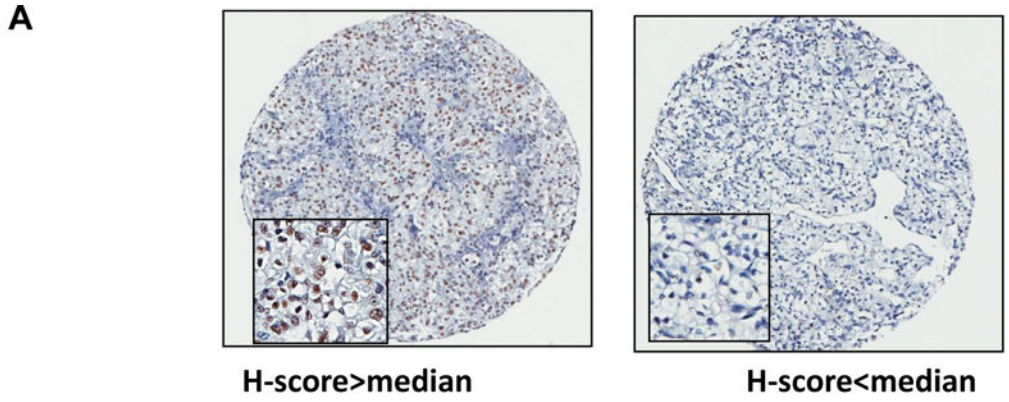

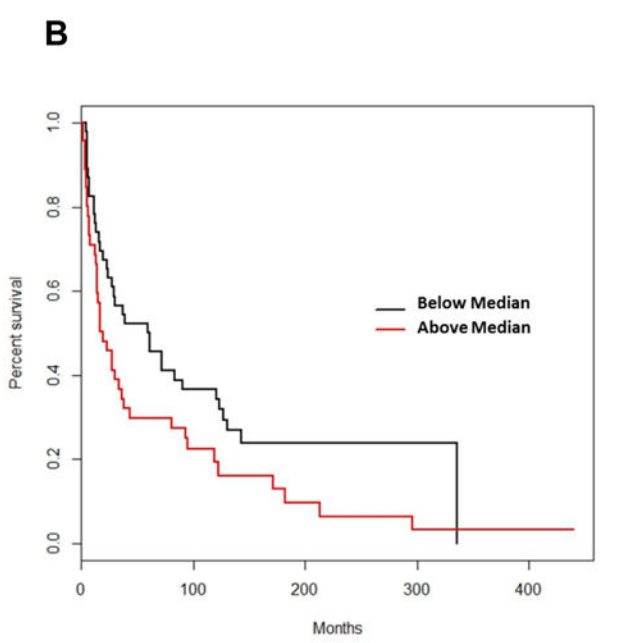

Hazard Ratio	1.6
pValue	0.05
Median OS, EZH2 high (H-score > median)	19 months
Median OS, EZH2 low (H-score < median)	60 months

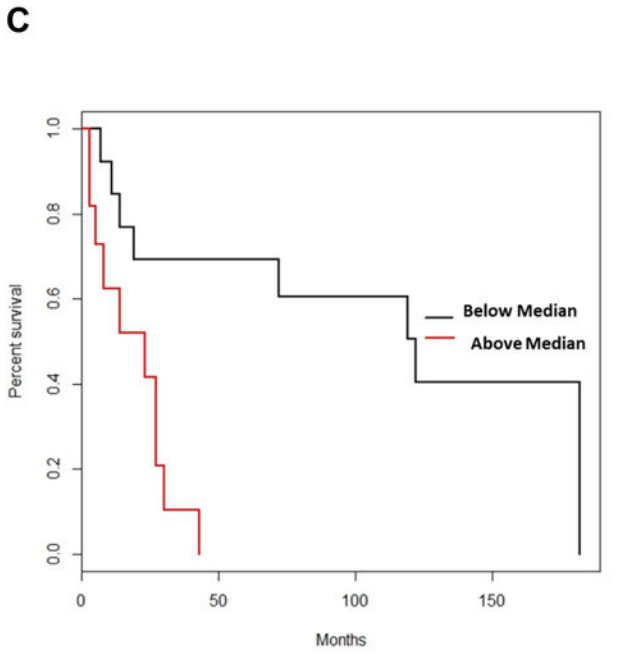

Hazard Ratio	5.6
pValue	0.005
Median OS, EZH2 high (H-score > median)	23 months
Median OS, EZH2 low (H-score < median)	122 months

Figure 7. EZH2 expression is associated with poor survival in ccRCC

(A) Immunohistochemistry analysis for EZH2 and H-score on 3 cores of primary and metastatic ccRCC. Representative pictures of either high (H-score >median) or low (H-score <median) EZH2 expression are shown. (B) The Kaplan-Meier survival curve indicates that the median overall survival for EZH2 expression “below median” is 60 months compared to “above median,” 19 months. The hazard ratio for above *vs* below (below as baseline) is 1.6, with 95% confidence interval as [1.0, 2.5] and p-value as 0.05. (C) Similarly, the OS of a subset of patients that received RTKI indicates median overall survival for “below median”

to be 122 months *vs* "above median" 23 months. The hazard ratio for above *vs* below (below as baseline) is 5.6, with 95% confidence interval as [1.7, 18.7] and p-value as 0.005.